A New Operational Northern Hemisphere Snow Water Equivalent Retrieval Algorithm for FY-3F/MWRI-II Based on Pixel-Based Regression Coefficients

Jianwei Yang, Lingmei Jiang, *Member, IEEE*, Zhaojun Zheng, Jinmei Pan, *Member, IEEE*,
and Anaer Shayiran

***Abstract*— Satellite passive microwave (PMW) remote sensing is widely used for monitoring the snow water equivalent (SWE) in the Northern Hemisphere. Existing operational SWE retrieval methods, especially those without assimilating ground-based snow depth priors, still utilize globally constant coefficients to construct regression-based retrieval algorithms. The current Fengyun-3 (FY-3) series of SWE product algorithms has made improvements in China, where biases have been significantly reduced locally but not in other regions. Within the context of the successful launch of the FY-3F satellites in 2023, we developed a better Northern Hemisphere algorithm for the Microwave Radiation Imager-II (FY-3F/MWRI-II) using pixel-sensitive coefficients regressed on a reference SWE dataset. We utilized the random forest model coupled with the snow emission model (HUT-RF) to obtain a high-accuracy SWE reference dataset. Then, we employed linear regression equations to fit the reference HUT-RF dataset at each pixel to construct the new operational FY-3F algorithms. We innovatively introduced the brightness temperature differences between 18.7 and 89 GHz and the polarization differences at 10.65 GHz in the regression after noting their sensitivity in deep snow estimation. The proposed FY-3F algorithm was extensively validated via four spatially independent datasets. The results demonstrated that the proposed FY-3F algorithm performed well in non-mountainous and sparsely forested areas, e.g., the overall unbiased root mean square error (unRMSE) values were 27.15 mm over Russia and 13.70 mm over China. High uncertainties still occurred in complex terrains and densely forested areas, e.g., the overall unRMSE values were 75.30 mm over Canada and 129.06 mm over western North America. The proposed FY-3F algorithm could improve global snow cover monitoring capabilities and enhance the complete and timely understanding of SWE changes.**

***Index Terms*—FY-3F/MWRI-II, passive microwave (PMW) remote sensing, pixel-sensitive retrieval algorithm, snow water equivalent (SWE).**

I. INTRODUCTION

THE snow water equivalent (SWE), a key metric related to water storage in snowpacks, greatly impacts agricultural production, hydropower generation, water supply, and natural disaster management applications [1], [2], [3], [4], [5], [6]. Spaceborne passive microwave (PMW) remote sensing is a valid tool for monitoring the seasonal SWE at the global scale because of its independence from solar illumination, penetrability of clouds, and sensitivity to dry snowpack [7], [8], [9]. However, a complete and timely understanding of the SWE in spatiotemporal mapping is still restricted by several factors, e.g., the widespread distribution of snow cover and high temporal dynamicity [10], [11], [12], [13], [14].

To date, several international agencies have created various global operational SWE products, such as the Advanced Microwave Scanning Radiometer for Earth (AMSR-E) Observing System product [15] managed by the National Aeronautics and Space Administration (NASA), the standard AMSR-E and Advanced Microwave Scanning Radiometer-2 (AMSR2) products of the Japan Aerospace Exploration Agency (JAXA) [16], and the Global Snow Monitoring for Climate Research (GlobSnow) SWE product [17], [18] published by the European Space Agency (ESA). The National Satellite Meteorological Center, managed by the China Meteorological Administration (CMA), also provides daily SWE monitoring in real time and has produced a family of daily global-scale records from 2011 to the present that rely on Microwave Radiation Imager (MWRI) instruments onboard the Fengyun-3B, -3C, and -3D (FY-3B/3C/3D) series satellites [19], [20]. The FY-3B SWE retrieval algorithm over China was designed for the FY-3B satellite. It is based on the semiempirical relationships between ground-based SWE measurements and brightness temperature (Tb) gradients, e.g., between 18.7 and 36.5 GHz, 10.65 and 18.7 GHz, and 18.7 and 89 GHz [19].

Received 11 January 2024; revised 25 May 2024 and 16 August 2024; accepted 26 September 2024. Date of publication 14 October 2024; date of current version 30 October 2024. This work was supported in part by the National Natural Science Foundation of China under Grant 42201346, in part by the National Key Research and Development Program of China under Grant 2021YFB3900104, and in part by the Fundamental Research Funds for the Central Universities under Grant 2021NTST02. *(Corresponding author: Lingmei Jiang.)*

Jianwei Yang and Lingmei Jiang are with the Faculty of Geographical Science, Beijing Normal University, Beijing 100875, China (e-mail: yangjw@bnu.edu.cn; jiang@bnu.edu.cn).

Zhaojun Zheng is with the National Satellite Meteorological Center (National Center for Space Weather), Key Laboratory of Radiometric Calibration and Validation for Environmental Satellites, China Meteorological Administration, Beijing 100081, China (e-mail: zhengzj@cma.gov.cn).

Jinmei Pan is with the National Space Science Center, Chinese Academy of Sciences, Beijing 100190, China (e-mail: panjm@aircas.ac.cn).

Anaer Shayiran is with Beijing Huayun Shinetek Science and Technology Company, Ltd., Beijing 100081, China.

Digital Object Identifier 10.1109/TGRS.2024.3479452

The FY-3B SWE retrieval algorithm accounts for the influence of various land cover types (e.g., forestland, grassland, farmland, and barren land) on the SWE. For example, in China, the snow depth of a specific pixel is a weighted result based on land cover fractions. After the launch of the FY-3C satellite in 2013, the FY-3B retrieval algorithm continued to be used for SWE mapping across China. To achieve global SWE monitoring for the FY-3B/3C satellites, the standard AMSR2 algorithm [16] has been directly used outside China. The AMSR2 algorithm accounts for forest effects on the SWE, expressed as a weighted result of the SWE values of the open and forest subpixels. Based on the previous validation, the FY-3B SWE retrieval algorithm tends to underestimate the SWE in Northeast China and Northwest China [19], [20], [21]. Therefore, after the launch of the FY-3D satellite in 2017, we applied a spatial partitioning strategy to develop SWE retrieval algorithms for Northeast China and Northwest China (hereafter referred to as the FY-3D SWE retrieval algorithm) [20]. In Northeast China, the FY-3D algorithm compensates for snow depth via the forest cover fraction. In Northwest China, cross-polarization differences in high and low frequencies at 18.7 and 36.5 GHz are adopted to explain the effect of snow metamorphism on the SWE.

Numerous studies have shown that the currently available operational FY-3D SWE retrieval algorithm faces certain challenges, such as different retrieval methods in China and outside China, most likely resulting in spatially distributed SWE patches. Moreover, the FY-3D SWE algorithm can underestimate snowpacks above 20 cm in China [20], [21] and overestimate shallow snowpacks below 5 cm [22]. Outside China, the FY-3D SWE retrieval method achieved similar performance as the standard AMSR2 product; for example, it is unresponsive to snow depth and seriously underestimates the global scale [23], [24].

In addition to the mixed-pixel problem in spaceborne PMW remote sensing, the main challenges in SWE retrieval include variable snow microstructures (e.g., snow density and snow grain size) and uncertain radiative interactions among snow, forest canopies, and the underlying soil. The inversion coefficients of widely used empirical algorithms are generally static. The basic assumption is that the snow microstructure is fixed; for example, a snow density of 300 kg/m^3 and a grain size of 0.3 mm were considered in Chang's method [8]. In fact, snow microstructures evolve throughout the snowy season. For example, the grain size can increase from 0.3 mm (fresh snow) to 4 mm (depth hoars), which results in different scattering effects. Moreover, static retrieval algorithms were developed based on the limited station-based measurements, in which the representativeness and proportionality of the training samples are problematic. The abovementioned factors generally result in poor applicability and robustness of the currently used operational retrieval methods. Although the standard AMSR2 algorithm adopts a dynamic polarization difference index to compensate for the retrieval biases caused by the snow microstructure, previous articles have demonstrated that this algorithm provides a slight advantage over typical static methods [16], [25], [26].

Another persistent question is the representativeness of ground truth measurements within 25 × 25 km satellite pixels. Most operational SWE retrieval methods were built based on empirical or semiempirical relationships between ground-based station measurements and satellite-observed brightness temperatures (point-to-pixel). However, whether these point observations represent snowpack in larger areas is unknown. Moreover, ground truth measurements are sparse, especially in complex mountains. Therefore, it is necessary to develop an SWE retrieval algorithm based on pixel-to-pixel training samples, partly to avoid scale issues [27].

Within the context of the artificial intelligence era, machine learning techniques have the potential for use in SWE prediction [26], [28], [29], [30], [31], [32], [33], [34], [35]. We also previously attempted to use the random forest (RF) approach to estimate snow depth across China [21]; the results demonstrated that transfer learning for machine learning approaches is problematic; namely, well-trained machine learning models in a given domain often exhibit poor performance when directly applied to other domains. This occurs because snowpack characteristics (grain size, density, and so on) are highly variable, while no predictor variable in machine learning indicates a change in snowpack features [36], [37]. To address this problem, we introduced a prior snowpack descriptor, i.e., the effective grain size optimized by the Helsinki University of Technology snow emission model (HUT), into the RF model to improve SWE estimation [38]. A spatially independent verification revealed that the proposed HUT-RF model outperforms the RF algorithm without involving the effective grain size. Although the HUT-RF approach relies heavily on ground-based snow depth priors to optimize the effective grain size, it can generate long time series of spatially continuous SWE products in the Northern Hemisphere, which is important for building a pixel-sensitive retrieval algorithm. Launched on August 3, 2023, the FY-3F satellite, which is a substitute for the FY-3C satellite, is equipped with second-generation MWRI (MWRI-II) sensors to provide global surface monitoring. Within this context, it is necessary to develop a new operational SWE retrieval algorithm for FY-3F/MWRI-II.

Overall, the objectives of this study are to 1) develop a pixel-sensitive SWE retrieval algorithm for FY-3F/MWRI-II in the Northern Hemisphere in which the inversion coefficients vary pixel by pixel (hereafter referred to as the FY-3F algorithm); 2) verify its performance via four spatially independent verification datasets; and 3) compare its SWE estimates with those of the widely used GlobSnow-v3.0 product. To our knowledge, this type of pixel-based algorithm built for the Northern Hemisphere is proposed for the first time. This study is structured into five sections. In Section II, the data used and the proposed methodology are introduced. The results are described in Section III. In Section IV, the algorithm-related sources of uncertainty are examined. Finally, conclusions are given in Section V.

II. DATA AND METHODOLOGY

A. PMW Remote Sensing Data

The FY-3F satellite managed by the CMA was launched on August 3, 2023. It is a satellite in sun-synchronous orbit

TABLE I

COMPARISON OF THE AMSR2 AND FY-3 SERIES PAYLOADS

Satellite	**GCOM-W1**	**FY-3B**	**FY-3C**	**FY-3D**	**FY-3F**
Sensor	AMSR2	MWRI-I	MWRI-I	MWRI-I	MWRI-II
Launch time (YYYY-MM)	2012-05	2010-11	2013-09	2017-11	2023-08
Incident angle (°)	55	53	53	53	53
Equator crossing time (local time zone) A: ascending; D: descending	A: 13:30 D: 01:30	A: 13:40 D: 01:40	A: 22:15 D: 10:15	A: 14:00 D: 02:00	A: 22:10 D: 10:10
Frequency (GHz) Footprint size (km×km)	6.925 (35×62) 7.3 (35×62) 10.65 (24×42) 18.7 (14×22) 23.8 (11×19) 36.5 (7×12) 89 (3×5)	10.65 (51×85) 18.7 (30×50) 23.8 (27×45) 36.5 (18×30) 89 (9×15)	10.65 (51×85) 18.7 (30×50) 23.8 (27×45) 36.5 (18×30) 89 (9×15)	10.65 (51×85) 18.7 (30×50) 23.8 (27×45) 36.5 (18×30) 89 (9×15)	10.65 (51×85) 18.7 (30×50) 23.8 (27×45) 36.5 (18×30) 50.3 (9×15) 52.6 (9×15) 53.2 (9×15) 53.7 (9×15) 89 (9×15) 118.7 (9×15)

with local descending overpasses at approximately 10:00 A.M. The MWRI-II instrument onboard the FY-3F satellite is a 22-channel, 13-frequency, H/V-polarization radiometer that senses microwave signals in the 10.65–118.75-GHz channels (Table I). Compared with the MWRI-I instruments onboard the FY-3C and -3D satellites, FY-3F/MWRI-II has enhanced observation abilities with additional channels (Table I) and improvements in calibration and positioning accuracy and observation sensitivity.

Owing to the limited availability of FY-3F/MWRI-II observations, alternative satellite data are necessary. Although the AMSR2 onboard the GCOM-W1 satellite has sensed Earth radiation from space since May 2012, its configuration differs from that of FY-3F/MWRI-II, e.g., incident angle, equator crossing time, and footprint size (Table I). Thus, the FY-3C/MWRI-I brightness temperature product (http://satellite.nsmc.org.cn) was used for development and validation because its configuration is similar to that of FY-3F/MWRI-II.

B. Training and Validation Datasets

We collected daily meteorological station measurements over global land areas from the Global Historical Climatology Network-daily (GHCN-daily) database [39]. In addition, data acquired from stations of the China Meteorological Data Service Center were used as supplemental data (http://data.cma.cn/en). The attribute elements of each station consist of the location name, latitude, longitude, maximum temperature, minimum temperature, and snow depth. Because snow depth is the most important parameter in this study, only weather stations (4485) that record snowfall are shown in Fig. 1(a). The measurements acquired from September 2013 to May 2022 were used for training to develop the FY-3F SWE retrieval algorithm.

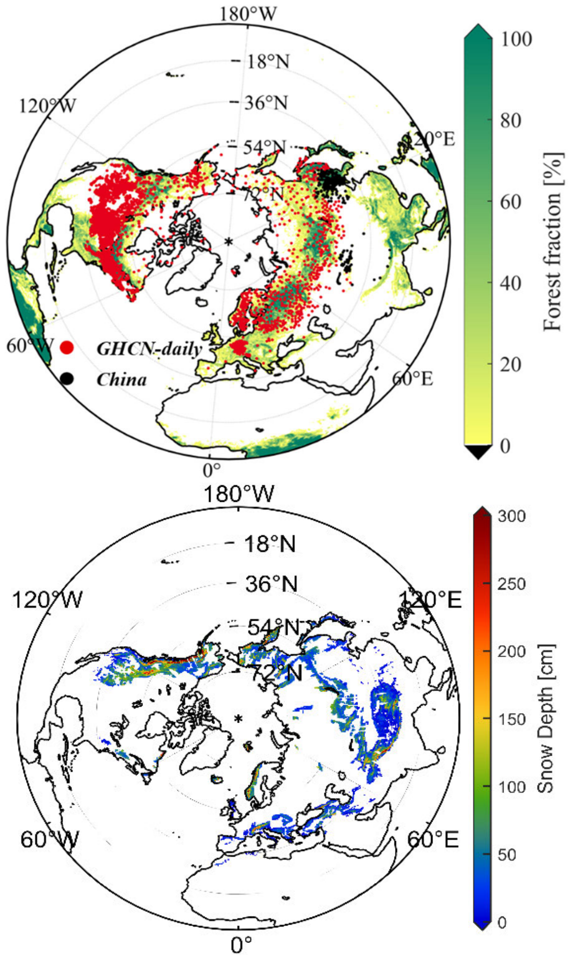

Fig. 1. (Top) Spatial distribution of the snow depth stations in the Northern Hemisphere. (Bottom) Base map is the forest fraction calculated based on the MODIS land cover product and the average snow depth of C-SNOW in January 2019.

The ground-based snow depth observations in complex topographic areas are sparse and even lacking. Previous studies have demonstrated that the C band is suitable for retrieving deep snowpacks (>100 cm) because low-frequency signals exhibit greater penetrability than high-frequency signals (e.g., the Ku band) do [40]. Thus, we selected synthetic aperture radar (SAR) Sentinel-1 snow depth retrievals (C-SNOW) during the 2016–2020 period to compensate for the lack of observations in the mountains [Fig. 1(b)]. C-SNOW snow depth retrievals were obtained over the Northern Hemisphere mountains, and the spatial resolution of the observations is ∼1 km [40], [41]. Here, only snow depth values greater than 100 cm were selected as training samples. One reason is that the C-band signal is sensitive to deep snow because of its strong penetration ability compared with that of the Ku band. Another reason is that nearly 90% of station-based snow depth samples range from 1 to 100 cm, and more deep snow conditions are necessary for training the machine learning model. Quality control was further conducted according to the product flags, for example, masking the values in densely vegetated areas, glaciated areas, and wet snow conditions. Here, C-SNOW retrievals outside Europe between September 2016 and August 2017 were also removed because of low accuracy associated with the reduced frequency of Sentinel-1 observations (only ascending or descending observations) [40]. To match the FY-3C pixel resolution, the C-SNOW product was resampled to a 25 × 25 km EASE-GRID size. All the C-SNOW snow depth values within an FY-3C pixel were averaged as ground truth data. Here, ground-based observations were used as truth data, and C-SNOW SWE values were used as candidates; namely, if the ground-based observations were lacking, C-SNOW snow depth data were then selected as truth data. To transfer snow depth to the SWE, a constant snow density of 240 kg/m^3 was used. The selected 16 800 C-SNOW SWE samples at 25 × 25 km EASE-GRID ranged from approximately 240–800 mm in this work and were mostly distributed in the Cordillera Mountains.

To assess the proposed FY-3F SWE algorithm, four spatially independent reference datasets distributed across Russia, North America, and China were collected, as listed in Table II.

1) Snow Survey Data for Russia: Snow surveys were conducted at 517 meteorological sites every five to ten days [42] during the snow season (green points in Fig. 2). The snow course was approximately 1–2 km long, the snow depth was recorded every 10–20 m, and a snow pit (snow density and snow temperature) was recorded every 100–200 m. After cross-checking various datasets, 44 snow courses overlapped with the GHCN-daily stations. To ensure that the Russia dataset was independent of the training samples, we removed these 44 snow courses from the Russia dataset. A total of 13 526 samples were collected from 2013 to 2018 as evaluation data in this study.

2) Canadian Historical Snow Water Equivalent Dataset: Canadian Historical Snow Water Equivalent (CanSWE) observations [43] were collected via various measurement methods, e.g., field campaigns (snow rulers or scales), snow pillows, passive gamma rays, Global Navigation Satellite System-Reflectometry (GNSS-R), and cosmic rays (light blue points in Fig. 2). The available variables were snow depth, snow density, and SWE. A total of 40 224 samples from 2013 to 2018 were used to verify the FY-3F SWE product in this study.

TABLE II

SUMMARY OF THE FOUR VALIDATION DATASETS

No.	**Dataset name**	**Time coverage**	**Number of snowpits or snow courses**	**Number of samples**
1	Snow course data from Russia	2013-2018	473	13,526
2	Snowpit data from Canada (CanSWE)	2013-2018	139	40,224
4	SWE data from western North America (SNOTEL)	2013-2018	660	257689
3	Snow field sampling in China	2018	425	78

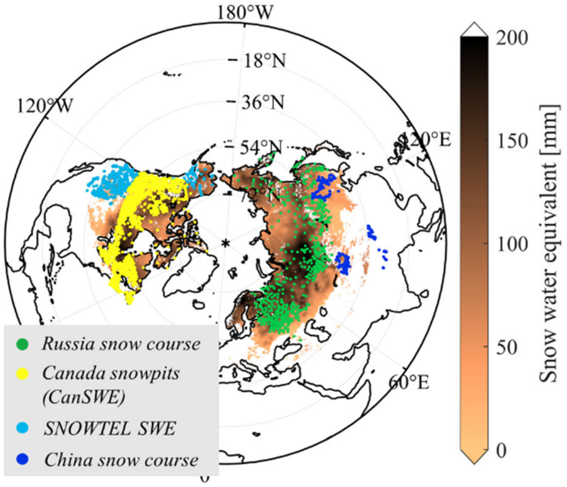

Fig. 2. Spatial distribution of the validation dataset locations in the Northern Hemisphere. The base map shows the GlobSnow-v3.0 monthly mean snow depth in March 2013.

3) Snowpack Telemetry Dataset: The snowpack telemetry (SNOTEL) stations are located mainly in the mountains of the United States and Canada, where the SWE is automatically acquired by snow pillows (yellow points in Fig. 2). The daily time series of SNOTEL records were obtained from the Natural Resources Conservation Service and National Water and Climate Center [44]. The raw SNOTEL datasets were systematically processed to address data quality concerns. In addition, we removed the 237 snowpits overlapping the GHCN-daily stations to ensure that the SNOTEL dataset was independent of the training samples. A total of 257 689

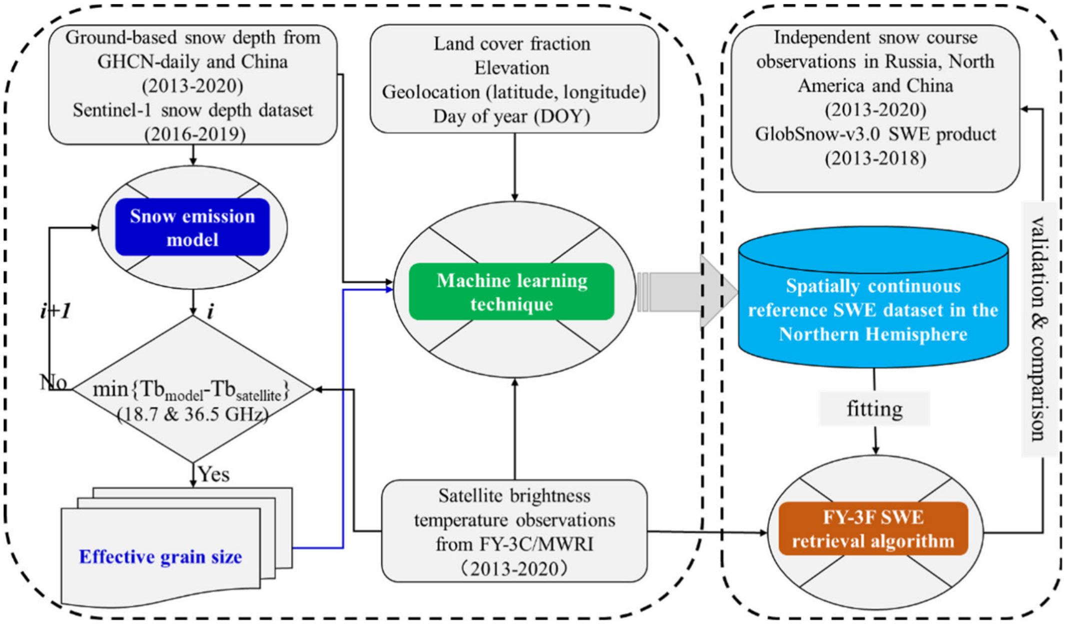

Fig. 3. Working chain of the FY-3F SWE retrieval algorithm.

samples from 2013 to 2018 were used to verify the FY-3F SWE algorithm in this study.

4) Dense Field Sampling Over China: A dense field campaign was performed across China to measure snow characteristics, including snow depth and snow density (blue points in Fig. 2), during the winter snow season of 2018 in Northeast China and northern Xinjiang. All the measurements (4–35) obtained from the FY-3C pixels (25 × 25 km) were averaged to obtain the ground truth values (from 5 to 100 mm). Seventy-eight satellite pixels were matched based on 425 field measurements in this study.

C. Other Auxiliary Data

The effect of the landscape on SWE retrieval has been explored in previous studies [19], [38], [45]. In this work, a MODIS Level 3 land cover product with a 500-m spatial resolution (MCD12Q1) was downloaded. Seventeen land cover classes were further regrouped into six categories: forestland, farmland, grassland, barren land, water bodies, and construction land. A land cover fraction map of the Northern Hemisphere at a 25 × 25 km resolution was generated based on the MCD12Q1 product. To reduce the influence of water and urban landscapes on the SWE estimates, the corresponding pixels (fraction $>$ 30%) were removed. The orographic effect also dominates snow accumulation, ablation, and redistribution [45], [46], [47], [48], [49]. Thus, the resampled Shuttle Radar Topography Mission (SRTM) digital elevation model (DEM) data with a 25 × 25 km spatial resolution were used in this study.

In this study, the GlobSnow-v3.0 effective grain size product was downloaded from www.globsnow.info [18], [50]. In the GlobSnow methodology, the snow depth interpolated with weather station measurements is applied as a prior field to optimize the effective grain size in the HUT model. Therefore, the GlobSnow effective grain size product was used directly in Section II-D.

D. Methodology

Fig. 3 shows a flowchart of the construction of the FY-3F SWE retrieval algorithm. Our previous studies demonstrated that combining the snow emission model and machine learning approach could greatly improve SWE estimation [38]. Therefore, the first step was to iteratively optimize the grain size via a snow forward model in this study (Fig. 3). To improve the computational efficiency, we directly selected GlobSnow-v3.0 effective grain size data as predictors for the RF model in this study. Then, an SWE retrieval method (HUT-RF) that couples the snow emission model (providing effective grain size) with the RF technique (possessing powerful fitting ability) was constructed (Fig. 3). Owing to the absence or incredibility of snow depth data in complex terrains, the Sentinel-1 C-SNOW dataset was used here. Afterward, the proposed HUT-RF model was used to produce a long-term spatially continuous SWE product (as a reference dataset). Eventually, the FY-3F algorithm was built for each snow-covered pixel based on the reference SWE dataset. A microwave snow cover detection method [51] was used to distinguish snow and snow-free pixels prior to SWE retrieval according to previous assessments [52], [53].

To demonstrate the performance of the proposed FY-3F algorithm, it was verified with various spatially independent SWE observations in Russia, North America, and China and was compared with the widely used GlobSnow-v3.0 product. Here, only the GlobSnow-v3.0 product was selected for comparison with our proposed FY-3F algorithm because existing publications have demonstrated that it is currently the most widely used and accurate operational remote sensing SWE product [18], [23], [24], [38].

1) Effective Grain Size Optimized by the Microwave Emission Model: In GlobSnow, a methodology that applies a snow microwave forward model to iteratively optimize the grain size was proposed [17]. In this method, synoptic ground-based snow depth values are used to drive the snow forward model to simulate the microwave brightness temperature of snow. Then, the differences between the model simulations and satellite observations at 18.7 and 36.5 GHz are minimized by iteratively optimizing the effective grain size. The fitting procedure is as follows:

$$\min_{d0}\left\{[\mathrm{Tb}_{18.7\mathrm{V,model}}(\mathrm{SD}_{\mathrm{ini}}, d0) - \mathrm{Tb}_{36.5\mathrm{V,model}}(\mathrm{SD}_{\mathrm{ini}}, d0)] - [\mathrm{Tb}_{18.7\mathrm{V,satellite}} - \mathrm{Tb}_{36.5\mathrm{V,satellite}}]\right\}^2 \tag{1}$$

where $\mathrm{Tb}_{\mathrm{pq,model}}$ denotes the brightness temperature simulations by using snow emission models, such as the HUT, the dense media radiative transfer (DMRT), and the microwave emission model of layered snowpacks (MEMLS). $\mathrm{Tb}_{\mathrm{pq,satellite}}$ denotes the satellite observations, e.g., FY-3C/MWRI in this study. d_0 is the optimized effective grain size according to the HUT and DMRT models and the effective correlation length according to the MEMLS model. $\mathrm{SD}_{\mathrm{ini}}$ denotes the ground-based snow depth as a background field. The iteration ranges of the grain size for the HUT and DMRT models were set to 0–4 and 0–2 mm, respectively, and 0–0.8 for the MEMLS model.

We previously compared the effective grain size optimized by the HUT, MEMLS, and DMRT models. We found that their optimized effective grain size data are highly correlated, although the DMRT model is a fully physically based model and the MEMLS model analytically calculates scattering coefficients via the improved band approximation (IBA). Thus, we consider that the GlobSnow effective grain size product optimized by the semiempirical HUT model is reliable.

We also studied snow depth retrieval algorithms in previous studies by coupling a snow physical model (e.g., the Snow Thermal model, SNTHERM) and a machine learning approach in the Northern Hemisphere [34]. The results revealed that the effective grain size at 36.5 GHz calculated from the SNTHERM multilayer snow profile simulations was correlated with the optimized effective grain size determined from the GlobSnow product, which explains the physical basis of the effective grain size and its relationship with the measured snow microstructure under natural conditions. Owing to the low computational efficiency of the SNTHERM model, the GlobSnow product was used to determine the effective grain size in this study.

2) Determination of the Predictor and Target Variables for the HUT-RF Model: The predictor variables include the brightness temperature at 10.65, 18.7, 36.5, and 89 GHz; land cover fraction (forestland, farmland, grassland, and barren land); elevation; latitude; longitude; day of year (DOY); and effective grain size (Table III). Owing to the coarse spatial resolution of the FY-3C/MWRI-I and FY-3F/MWRI-II data, a pixel typically consists of several land cover types, e.g., grassland, cropland, barren land, and forestland. Previous studies have indicated that land cover type influences snow distribution and changes the snow microstructure [26], [38]. Moreover, topography (e.g., elevation) and geographic location (latitude and longitude) dominate snow spatial patterns [47], [48], [49]; for example, deep snow typically occurs in high-elevation or high-latitude areas. The DOY reflects the seasonal snow cover characteristics; for example, the SWE and grain size typically increase during the snow accumulation period. Therefore, the land cover fraction, elevation, latitude, longitude, and DOY were selected as predictor variables (Table II).

Microwave signals are sensitive to dry snowpack because of volume scattering caused by snow particles. Thus, brightness temperature gradients are typically used to retrieve the SWE. Theoretically, $\mathrm{Tb}_{18.7\mathrm{V}}$ is subjected to more snow metamorphism and forest than $\mathrm{Tb}_{10.65\mathrm{V}}$ [54]. Thus, $\mathrm{Tb}_{10.65\mathrm{V}}$-$\mathrm{Tb}_{36.5\mathrm{V}}$ was selected for this study. $\mathrm{Tb}_{89\mathrm{V}}$ is sensitive to relatively shallow snowpacks because of its low penetrability [19]. Typically, microwave emission at 89 GHz dominates the brightness temperature. Interestingly, our analysis revealed that $\mathrm{Tb}_{18.7\mathrm{V}}$-$\mathrm{Tb}_{89\mathrm{V}}$ presented a negative response to SWE (see Section IV). Thus, $\mathrm{Tb}_{18.7\mathrm{V}}$-$\mathrm{Tb}_{89\mathrm{V}}$ was selected as one predictor variable. The presence of deep snow and coarse particles (e.g., depth hoars) can result in notable volume scattering of snowpacks to microwave signals. Thus, depolarization effects typically occur. According to previous studies [12], [16], [38], [49] and our tests (see Section IV), the polarization difference is sensitive to snow metamorphism (e.g., grain size) and snow depth; therefore, $\mathrm{Tb}_{10.65\mathrm{V}}$-$\mathrm{Tb}_{10.65\mathrm{H}}$ was further selected as a predictor variable in this study.

For the RF machine learning model, two key parameters need to be determined: the number of decision trees (*n*tree) in the ensemble and the number of predictor variables (*m*try) randomly selected at each node. In this study, *n*tree was set to 500, which was sufficient for error convergence, and *m*try was 4, approximately one-third of the predictor variables (Table III). The training sample size was 247 800, including ground-based records from the GHCN-daily and Chinese stations and C-SNOW snow depth estimates (Table III). The spatially independent validation datasets are shown in Table II. See the details in Section II-B. The well-trained HUT-RF model was subsequently applied to produce a snow depth reference dataset for the Northern Hemisphere during the 2013–2020 period. The spatial independence of the HUT-RF model is verified in Section III-B.

3) Design of the FY-3F-SWE Retrieval Algorithm: One advantage of the HUT-RF model is that it can provide a historically long-term spatially continuous SWE dataset in the Northern Hemisphere, which can be used as reference SWE values due to the inclusion of ground-based measurements (Fig. 3). To achieve operational application for snow monitoring, a pixel-sensitive algorithm for FY-3F regression based on the HUT-RF reference dataset was utilized. The format of the proposed FY-3F algorithm is similar to that of the traditional empirical equation, but the fitting coefficients are dynamic on a pixel-by-pixel basis. Owing to the available typical frequencies (10.65, 18.7, 36.5, and 89 GHz) for FY-3F/MWRI-II and their sensitivity to the SWE (see Table III),

TABLE III

PREDICTOR AND TARGET VARIABLES FOR THE HUT-RF MODEL

Predictors	**Interpretation**	**Response**	**Data source**	**Target variable**	**Configuration**
$Tb_{10.65V}$-$Tb_{36.5V}$	Vertical polarized spectral difference at 10.65 and 36.5 GHz	positive to SWE	FY-3C/MWRI-I	Snow depth from GHCN-daily and China stations and C-SNOW snow depth retrievals greater than 100 cm (2013–2020)	*ntree*=500 *mtry*=4 *n*=247,800 (including 230,000 station-based records and 16,800 C-snow estimates)
$Tb_{18.7V}$-Tb_{89V}	Vertical polarized spectral difference at 18.7 and 89 GHz	sensitive to SWE	FY-3C/MWRI-I		
$Tb_{10.65V}$-$Tb_{10.65H}$	Vertical polarization difference at 10.65 GHz	Snow metamorphism and deep snow	FY-3C/MWRI-I		
DOY	Day of year	Temporal pattern	Calculated from year, month, and day		
Elevation	Altitude in meters	Spatial distribution	http://srtm.csi.cgiar.org		
Longitude/latitude	Geolocation in degrees	Spatial distribution	EASE GRID projection		
Land cover fraction	Grassland, cropland, barren land, and forestland	Spatial distribution	https://ladsweb.modaps.eosdis.nasa.gov/		
Effective grain size	An effective value optimized by the HUT model	Snow metamorphism	GlobSnow-v3.0 (https://www.globsnow.info/)		

we constructed a multiband retrieval algorithm. The format of the proposed FY-3F algorithm is as follows:

$$\begin{aligned}\mathrm{SWE} = {} & \mathrm{slope1} \times (\mathrm{Tb}_{10.65\mathrm{V}} - \mathrm{Tb}_{36.5\mathrm{V}}) \\ & + \mathrm{slope2} \times (\mathrm{Tb}_{18.7\mathrm{V}} - \mathrm{Tb}_{89\mathrm{V}}) \\ & + \mathrm{slope3} \times (\mathrm{Tb}_{10.65\mathrm{V}} - \mathrm{Tb}_{10.65\mathrm{H}}) + \mathrm{intercept} \qquad (2)\end{aligned}$$

where $Tb_{10.65V}$, $Tb_{18.7V}$, $Tb_{36.5V}$, and Tb_{89V} denote the brightness temperatures at vertical polarizations ranging from 10.65 to 89 GHz, and SWE is the estimated SWE. Slope and intercept coefficients were calculated by fitting the Tb differences and SWE values retrieved by HUT-RF at each snow-covered pixel. The basic principles for selecting $Tb_{10.65V}$-$Tb_{36.5V}$, $Tb_{18.7V}$-Tb_{89V}, and $Tb_{10.65V}$-$Tb_{10.65H}$ are shown in Table III. We also tested the roles of the three Tb differences in (2). Refer to Section IV for more details.

III. RESULTS

A. Development of the FY-3F SWE Retrieval Algorithm

Based on the snow depth reference dataset for the Northern Hemisphere during the 2013–2020 period, the slope and intercept coefficients of function (2) were fit pixel by pixel. Fig. 4 shows the spatial distributions of slope1, slope2, slope3, and the intercept in the Northern Hemisphere. The relationships between the satellite-based observations and the reference snow depth were determined by slope1, slope2, and slope3. These fitting coefficients exhibited high spatial heterogeneity (Fig. 4). Slope1 reflects the role of $Tb_{10.65}$ and $Tb_{36.5}$ in retrieving snow depth and indicates patterns similar to those of snow depth and terrain. The thicker the snow cover is, the greater the slope is. For slope2, the role of $Tb_{18.7}$ and Tb_{89} in retrieving the snow depth is notable above a northern latitude of 50. Slope3 denotes the role of the polarization difference at 10.65 GHz ($Tb_{10.65V}$-$Tb_{10.65H}$) in retrieving the snow depth; it exhibits similar patterns as slope1, indicating that it compensates for snow depth estimates. A more detailed discussion is given in Section IV.

The intercept denotes the systematic biases. Assuming that the fitting relationship between the SWE and satellite observations is robust, the intercept should equal zero when snow is free based on scattering theory. However, deep snowpack, snow metamorphism, and forest landscapes generally lead to saturation effects resulting from microwave signals. Within

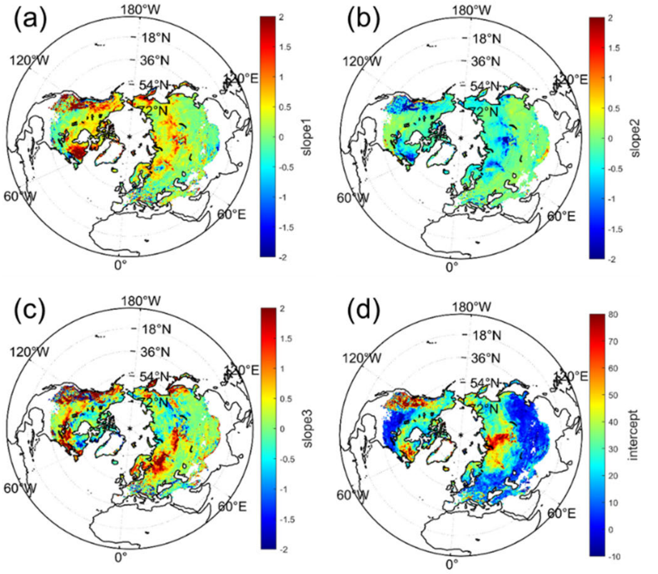

Fig. 4. Spatially dynamic fitting coefficients of (a) slope1, (b) slope2, (c) slope3, and (d) intercept for the FY-3F snow depth retrieval algorithm in the Northern Hemisphere.

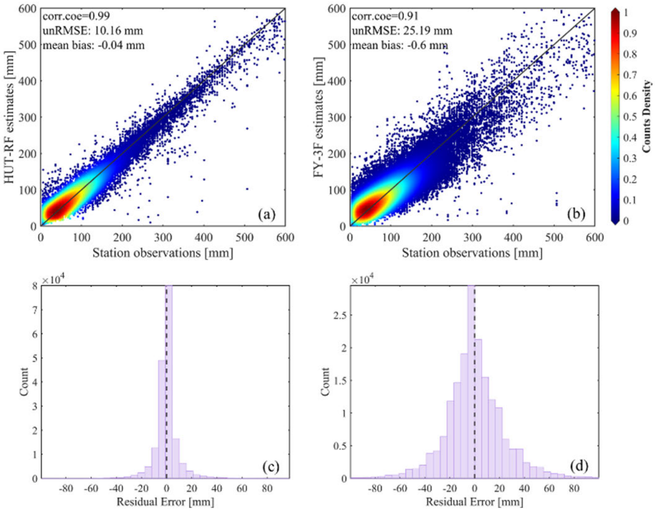

Fig. 5. Comparison of the station-based SWE data with (a) HUT-RF model and (b) FY-3F algorithm results. (c) and (d) Residual error plots for the HUT-RF model and FY-3F algorithm, respectively.

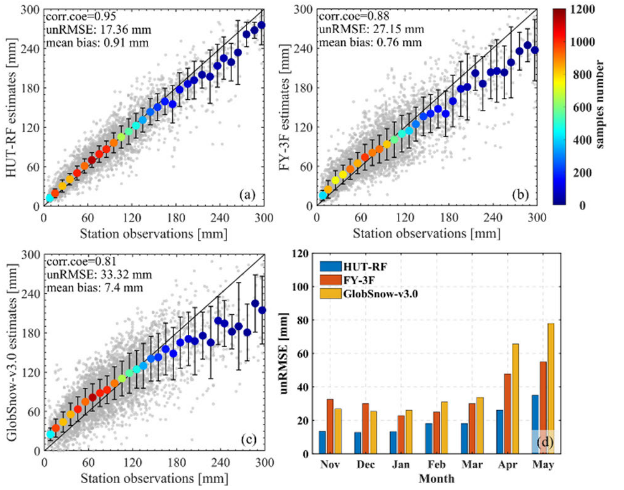

Fig. 6. Validation of (a) HUT-RF, (b) FY-3F, and (c) GlobSnow-v3.0 SWE estimates over Russia (snow course) and (d) comparison with respect to unRMSE.

this context, the intercept can partially correct the errors under low- and high-end snowpack conditions and improve snow depth estimates overall. As shown in Fig. 4, the intercept coefficient is generally high under deep snow conditions, such as above 50°N, and in the Canadian Rocky Mountains and the Coast Mountains, whereas it is negative in shallow snow cover areas, which are lower than approximately 50°N. Here, the microwave snow identification method proposed by Dozier et al. [47] was used to detect dry snow according to a previous assessment [48], [49].

Fig. 5 shows a comparison of the station-based snow depth values with the HUT-RF and FY-3F model estimates in the Northern Hemisphere. The HUT-RF model outperformed the developed FY-3F algorithm; for example, the HUT-RF model yielded the unbiased root mean square error (unRMSE) values of 10.16 and 25.19 mm. Fig. 5 shows the histograms of the residual errors of these two models, which clearly exhibit a normal distribution. For the HUT-RF model, 90% of the biases varied between −10 and 10 mm, indicating that the reference snow depth dataset based on the HUT-RF model is reliable. For the FY-3F algorithm, most residual errors varied between −30 and 30 mm. The spatial independence verification of the HUT-RF model and FY-3F algorithm is described in Section III-B.

B. Validation and Comparison of the SWE Estimates

Four spatially independent datasets were selected to verify the performance of the HUT-RF model and FY-3F SWE retrieval algorithm in the Northern Hemisphere. Moreover, these products were compared with the widely used GlobSnow-v3.0 product. Fig. 6 shows the validation and comparison results for the HUT-RF, FY-3F, and GlobSnow-v3.0 SWE estimates over Russia. Overall, the HUT-RF model performed best among these three algorithms. The FY-3F and GlobSnow-v3.0 estimates yielded similar unRMSE (27.15 and 33.32 mm, respectively) and correlation coefficient (0.81 and 0.88, respectively) values. Fig. 6(d) shows the monthly performances of the above three retrieval algorithms and products. The unRMSE increased during the snowy season from November to the following May. The FY-3F and GlobSnow-v3.0 SWE estimates from November to March agreed well but differed between April and May. One reason is that there were few available station measurements during the late snowy season, which resulted in high uncertainty in the interpolated effective grain size of the HUT model. Therefore, the GlobSnow-v3.0 product achieved poor performance in April and May.

Fig. 7 shows the validation and comparison results for the HUT-RF, FY-3F, and GlobSnow-v3.0 SWE estimates over Canada. The ground snow pits in Canada are mostly distributed in complex mountains and forest-covered areas where snow cover is typically thick (up to 700 mm). Thus, the overall performance of these three algorithms was lower than that in Russia (Figs. 6 versus 7, respectively). Even for the HUT-RF

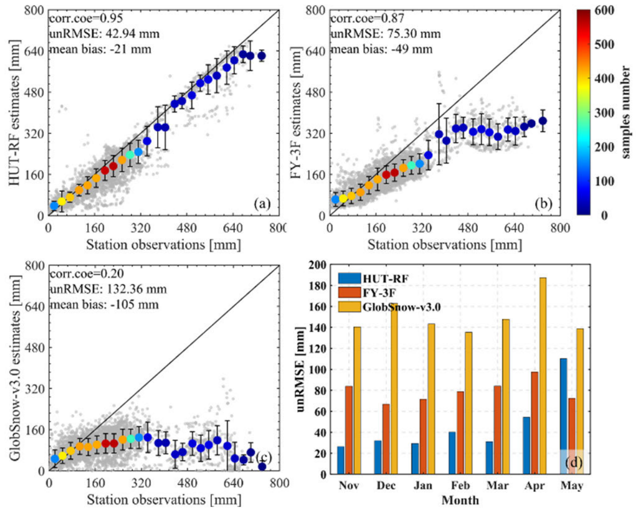

Fig. 7. Validation of (a) HUT-RF, (b) FY-3F, and (c) GlobSnow-v3.0 SWE estimates and (d) comparison with respect to unRMSE over North America (Canada snowpits).

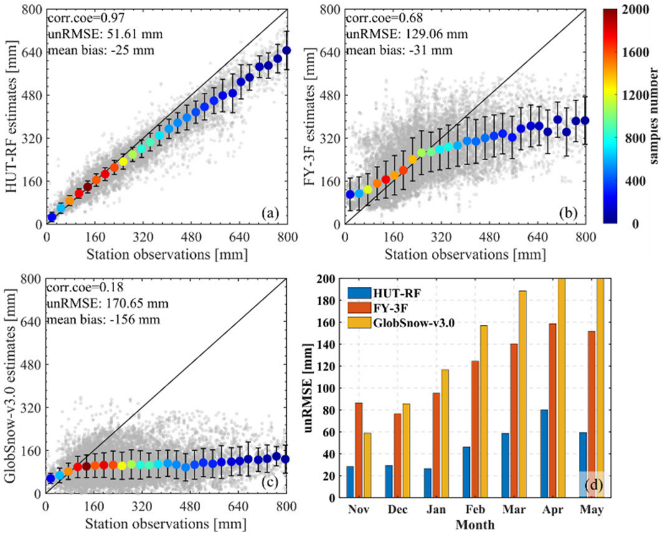

Fig. 8. Validation of (a) HUT-RF, (b) FY-3F, and (c) GlobSnow-v3.0 SWE estimates and (d) comparison with respect to the monthly unRMSE over North America (SNOTEL snowpits).

model, the unRMSE and bias values reached 42.94 and −21 mm, respectively. The FY-3F algorithm also yielded large errors (unRMSE of 75.3 mm) and severe underestimations (bias of −49 mm). A discussion is provided in Section IV. The GlobSnow-v3.0 product has no response to SWE variation, indicating that it is not applicable in complex terrain areas. Fig. 8(d) shows the monthly performance of these three algorithms. The unRMSE of the HUT-RF model increased during the snowy season from November to the following May. However, the FY-3F and GlobSnow-v3.0 SWE algorithms all presented high unRMSE values throughout the entire snowy season, especially for the GlobSnow-v3.0 product.

Fig. 8 shows the validation and comparison results for the HUT-RF, FY-3F, and GlobSnow-v3.0 SWE estimates over western North America. The SNOTEL stations were designed for remote and complex mountains (e.g., the Canadian Rocky Mountains and the Coast Mountains), where the SWE is typically up to 1000 mm (Fig. 2). The HUT-RF model performed well, with the unRMSE and bias values of 51.61 and −25 mm, respectively, which contributed to the predictor variables of the effective grain size, elevation, and forest fraction and the target variable, in which Sentinel-1 snow depth observations were involved (Fig. 1). The FY-3F algorithm exhibited high uncertainty, with an unRMSE value of up to 129.06 mm. The GlobSnow-v3.0 product exhibited almost no response to SWE changes. Fig. 8(d) shows the monthly performance of these three algorithms. Even for the HUT-RF model, the unRMSE value reached 80 mm in May. For the FY-3F and GlobSnow-v3.0 SWE algorithms, the estimates notably deviated from the station measurements.

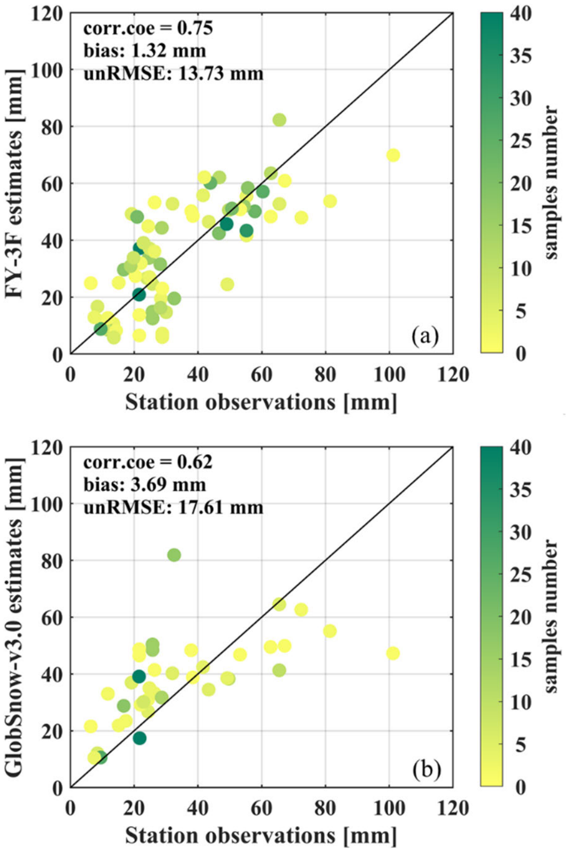

Fig. 9. Validation and comparison of (a) FY-3F and (b) GlobSnow-v3.0 SWE estimates across China (field sampling).

Fig. 9 shows the validation and comparison results for FY-3F and GlobSnow-v3.0. SWE estimates over China. The color bar indicates the sample number in the satellite pixels. The results revealed that the FY-3F algorithm yielded results similar to those of the GlobSnow-v3.0 product, with the unRMSE (corr.coe) values of 13.73 (0.75) and 17.61 (0.62) mm, respectively.

C. Spatial Distribution and Monthly Performance

Fig. 10 shows the monthly spatial distributions of the FY-3F and GlobSnow-v3.0 SWE estimates in the Northern Hemisphere. The results indicated a basically consistent spatial pattern between the FY-3F and GlobSnow-v3.0 estimates.

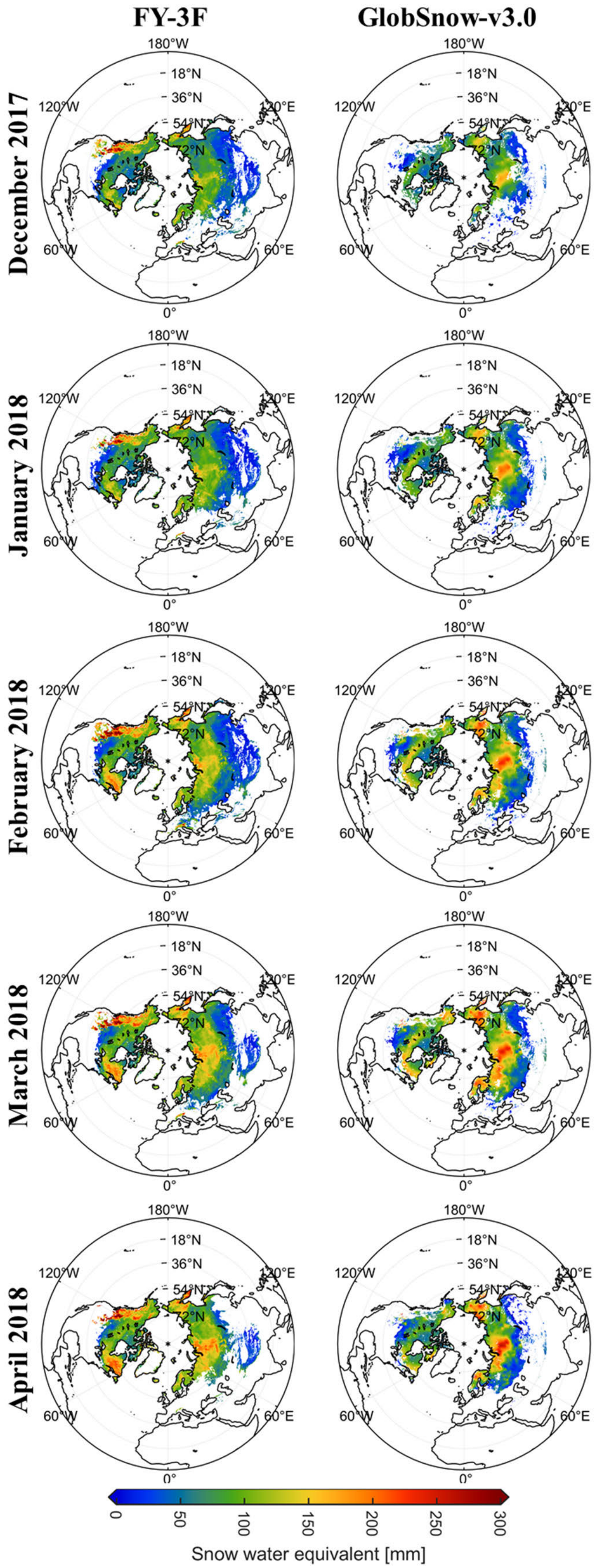

Fig. 10. Monthly distributions of the FY-3F and GlobSnow-v3.0 SWE estimates in the Northern Hemisphere.

Most complex mountains are masked in the GlobSnow-v3.0 product because ground-based snow depth measurements are rare. Thus, the snow cover areas in the GlobSnow-v3.0 estimates were evidently smaller than those in the FY-3F estimates. Here, the different microwave snow identification methods used in the GlobSnow-v3.0 and FY-3F methods also influenced the obtained snow cover areas.

Owing to the high uncertainties of SWE estimates over complex terrains, current PMW products typically mask SWE estimates in mountainous regions, e.g., the GlobSnow-v3.0 product. Fig. 11 shows the monthly spatial distributions of the FY-3F SWE estimates in the Canadian Rocky Mountains, High Mountain Asia, and East Siberian Mountains. Although spatially independent validation revealed that the FY-3F algorithm exhibited high uncertainty over complex mountains (Figs. 7 and 8), it could reflect the spatial patterns of the SWE and provide spatially continuous SWE mapping, except for some water bodies (Fig. 11). The SWE was typically high in mountainous areas relative to flat areas. Moreover, the SWE gradually increased from December 2017 to April 2018.

IV. Discussion

In this study, the HUT-RF model was used to provide spatially continuous reference snow depth data for building the FY-3F SWE retrieval algorithm. Generally, both the grain size and the SWE influence the optical thickness of snow. Thus, their coupling increases the complexity of SWE retrieval via empirical and semiempirical methods. In the HUT-RF model, the effective grain size optimized by the HUT model is involved, partially enhancing the predictive power of the machine learning approach. Moreover, the land cover fraction, elevation, and DOY variables are considered in the HUT-RF model, which partially reduces the influence of the terrain and forests on the SWE estimates [38]. In addition, machine learning techniques present greater potential in fitting multivariate nonlinear relationships between predictor variables and SWE than traditional statistical regression methods do. Thus, the HUT-RF retrievals are partially reliable as a reference dataset for building the FY-3F SWE retrieval algorithm (Figs. 6–8).

However, HUT-RF is not a physics-based model that can clarify the radiative transfer process of layered natural media (e.g., soil, snow, forest, and atmosphere) or their interactions. Thus, uncertainties remain in some areas, although the overall performance of the HUT-RF model is promising. For example, especially for the late snow season (April and May), the unRMSE values ranged from 30 to 110 mm [Figs. 6(d)–8(d)]. This is partially due to the saturation of PMW signals caused by liquid water in wet snow conditions, which affects the SWE estimates [13]. Another reason is that the frequent melt-free snow events in late snow seasons lead to snow grain growth [12], which increases the volume scattering of snowpack (Figs. 7–8).

Another noteworthy issue is the representativeness and imbalance of training samples for machine learning models. In this work, the target variable for training the RF-HUT model was acquired from weather stations, while its representativeness in a coarse pixel remains to be evaluated, especially in complex mountains and densely forested areas [27]. Moreover, most stations are distributed in flat and open areas where the

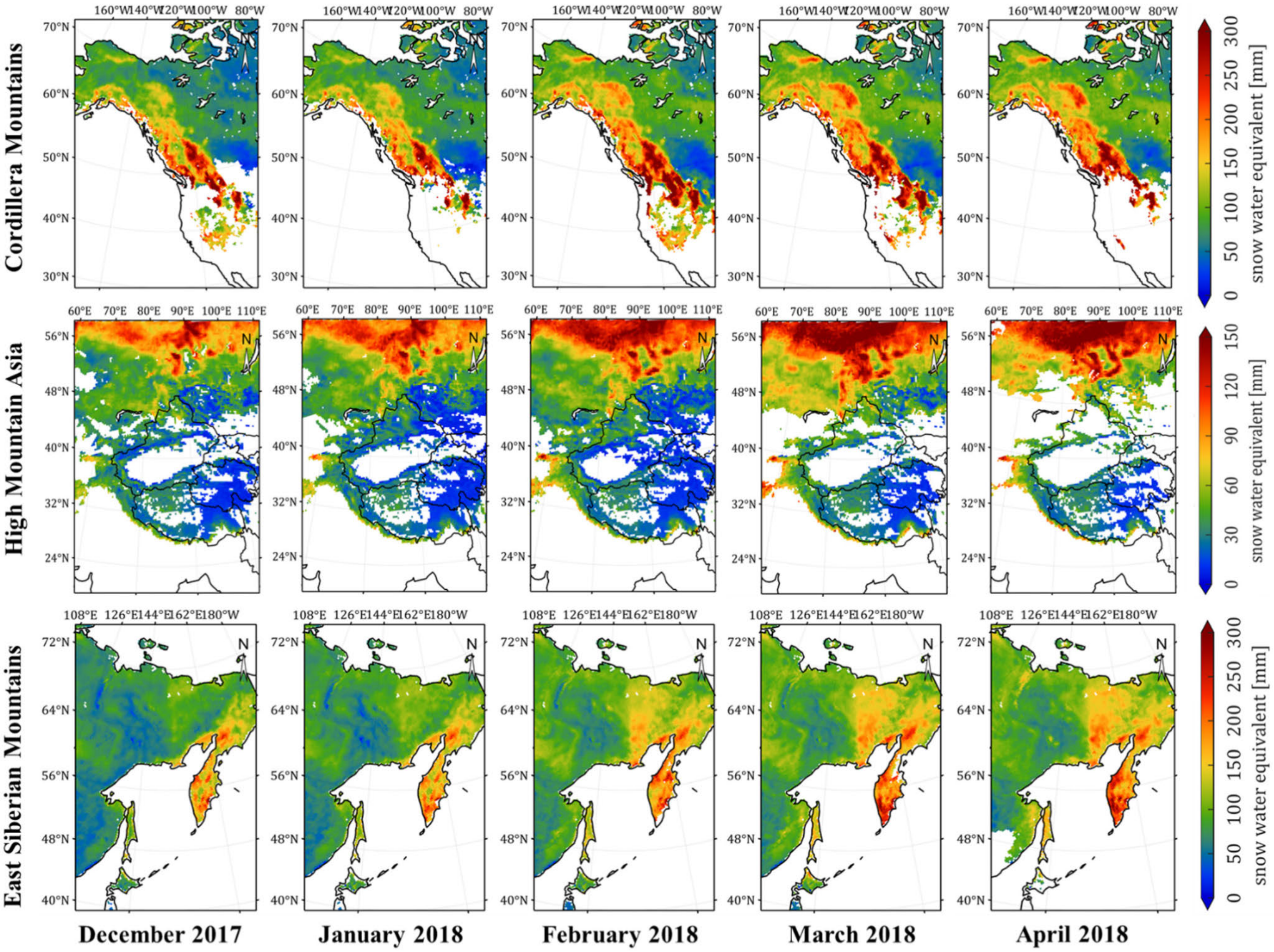

Fig. 11. Monthly distributions of the FY-3F SWE estimates in the Cordillera Mountains, High Mountain Asia, and East Siberian Mountains.

snow depth is typically shallow compared with that in complex terrain areas. Thus, approximately 90% of the snow depth records range from 1 to 100 cm. Although Sentinel-1 snow depth data are considered in the RF-HUT model to enhance the balance of training samples, their retrievals in deep snowpack areas also present high errors in complex areas (wet snow and forest canopies) and fewer Sentinel-1 observation areas (e.g., North America and Asia), where repeat cycles occur every 6–12 days [40], [41]. Thus, imbalanced training samples also decrease the predictive power of machine learning.

The overall uncertainties in the HUT-RF estimates [the dependent variables in function (2)] can be propagated into the FY-3F algorithm; for example, its unRMSE values range from 50 to 160 mm, even exceeding 50% of the relative error [Figs. 6(d)–8(d)]. In future work, improving the understanding of the representativeness of reference SWE values and enhancing the balance of training samples by means of airborne SAR observations (a combination of C-band, X-band, and Ku-band data), automatic measurement networks, e.g., GNSS-R, satellite altimetry, light detection and ranging (LiDAR), and large model simulations (a combination of snow physical models and deep learning techniques), could contribute to the development of robust SWE retrieval algorithms and more accurate validation of SWE products.

Fig. 12 shows the overall relationship between the brightness temperature differences and the observed SWE values derived from the Russia, CanSWE, and SNOTEL datasets. $Tb_{10.65V}$-$Tb_{36.5V}$ exhibited a nonlinear relationship with the ground-based SWE data, first increasing from 0 to 100 mm and then decreasing above 100 mm. $Tb_{18.7V}$-Tb_{89V} indicated a downward trend for 0–200 mm snowpacks over Russia and 0–400 mm snowpacks over Canada, indicating greater sensitivity to the SWE than $Tb_{10.65V}$-$Tb_{36.5V}$. At 89 GHz, microwave emission dominates the brightness temperature, whereas volume scattering dominates radiation at 18.7 GHz. Thus, $Tb_{18.7V}$-Tb_{89V} decreases with increasing SWE. Over Eurasia, the polariton difference $Tb_{10.65V}$-$Tb_{10.65H}$ exhibited an upward trend for 0–100 mm snowpacks [Fig. 12(a)]. This is because vertically polarized signals have stronger penetration ability than horizontally polarized signals do. In Canada, $Tb_{10.65V}$-$Tb_{10.65H}$ exhibited a downward trend for 0–400 mm snowpacks [Fig. 12(b)]. This phenomenon is related to both the SWE and forest cover. The CanSWE dataset shows that the SWE increases with increasing forest fraction (Fig. 13). Thus, the volume scattering effects caused by the forest canopy and snowpack reduce the polariton difference, namely, the depolarization effect.

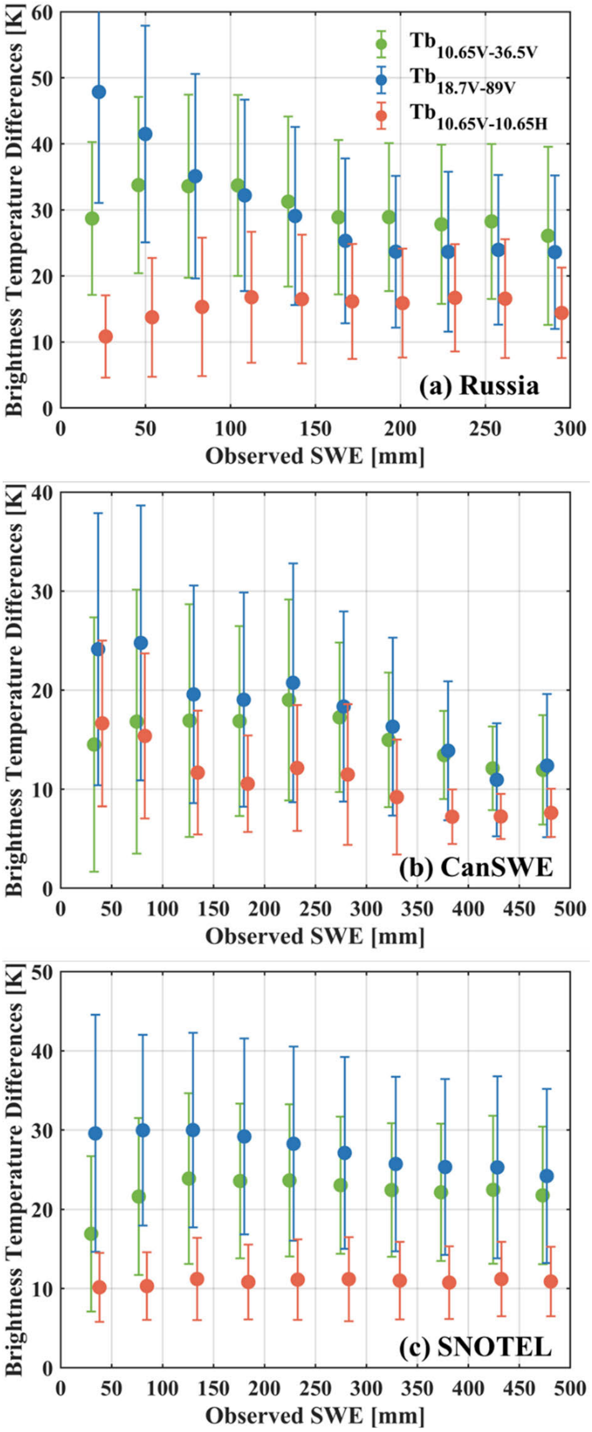

Fig. 12. Overall relationships between the brightness temperature differences and observed SWE values derived from (a) Russia, (b) CanSWE, and (c) SNOTEL datasets. The error bars and colored solid dots indicate the standard deviation and average value, respectively, of the brightness temperature data in specific SWE ranges.

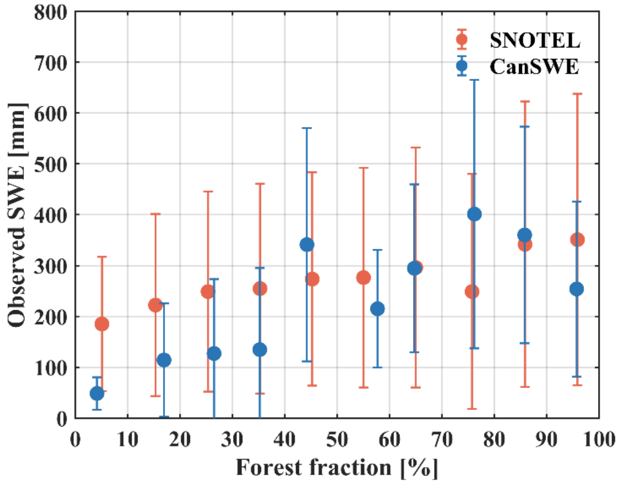

Fig. 13. Relationships between the forest fraction data and observed SWE values derived from the CanSWE and SNOTEL datasets.

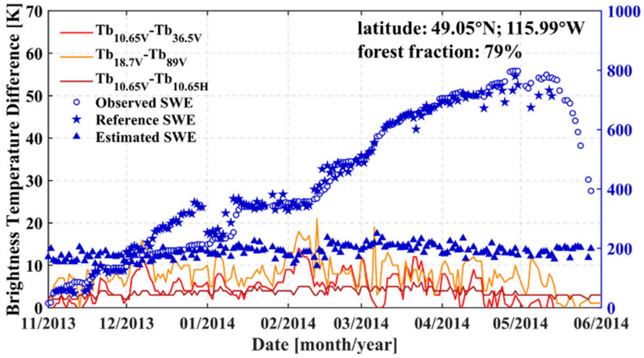

Fig. 14. Time series of the brightness temperature differences and SWE values (SNOTEL) in the forest areas.

Fig. 12(c) shows that the brightness temperature differences of $Tb_{18.7V}$-Tb_{89H} and $Tb_{10.65V}$-$Tb_{10.65H}$ were insensitive to the SWE for the SNOTEL dataset. This can be explained by the dense distribution of forest landscapes and the large amount of snow [40] in the Canadian Rocky Mountains and the Coast Mountains. Fig. 14 shows a case study of the time series brightness temperature differences and SNOTEL SWE values in a forested satellite pixel. The reference period was from November 2013 to May 2014 because of the continuous and greater number of observations relative to those in other periods. The hollow circles denote ground-based SWE values, and the pentagram-shaped and triangular solid dots denote the reference (HUT-RF model) and estimated (FY-3F) SWE data, respectively. The ground-based and reference SWE values increased from November 2013 to May 2014, whereas the brightness temperature differences were mostly insensitive to SWE changes, which led to severe underestimation by the FY-3F SWE retrieval algorithm (Figs. 7, 8, and 14). This occurred because dense forest cover (79%) masks microwave radiation stemming from snowpacks and soil. Forest canopy emissions are relatively stable during snowy winter seasons because of the low water content of vegetation and frozen ground. Therefore, notable volume scattering of the canopy and snow reduces the difference in $Tb_{10.65V}$-$Tb_{10.65H}$.

To determine the roles of $Tb_{10.65V}$-$Tb_{36.5V}$, $Tb_{18.7V}$-Tb_{89V}, and $Tb_{10.65V}$-$Tb_{10.65H}$ in the pixel-sensitive retrieval algorithm, three scenarios were further tested (Table IV). In Scenario 1, only $Tb_{10.65V}$-$Tb_{36.5V}$ was used to fit the slope and intercept for each pixel. In Scenarios 2 and 3, two brightness temperature gradients, $Tb_{18.7V}$-Tb_{89V} and $Tb_{10.65V}$-$Tb_{10.65H}$, were added step by step to regress with the SWE. The spatially independent validation results revealed that $Tb_{18.7V}$-Tb_{89V} and

TABLE IV
SUMMARY OF THE PERFORMANCES OF THE THREE RETRIEVAL ALGORITHMS

Retrieval algorithm	Russia			CanSWE			SNOTEL		
	Corr.coe	unRMSE (mm)	Bias (mm)	Corr.coe	unRMSE (mm)	Bias (mm)	Corr.coe	unRMSE (mm)	Bias (mm)
SWE=a*($Tb_{10.65V}$-$Tb_{36.5V}$)+b	0.85	30.6	-0.60	0.81	78.1	-52	0.68	127.7	-29
SWE=a*($Tb_{10.65V}$-$Tb_{36.5V}$)+b*($Tb_{18.7V}$-Tb_{89V})+c	0.88	27.4	0.13	0.87	76.9	-50	0.65	129.8	-31
SWE=a*($Tb_{10.65V}$-$Tb_{36.5V}$)+b*($Tb_{18.7V}$-Tb_{89V})+c*($Tb_{10.65V}$-$Tb_{10.65H}$)+d	0.88	27.2	0.80	0.87	75.3	-49	0.68	127.4	-28

$Tb_{10.65V}$-$Tb_{10.65H}$ improved the SWE estimates over Eurasia (Russia dataset), for example, with unRMSE values ranging from 30.6 to 27.4 and 27.2 mm, respectively. Over North America, the CanSWE dataset, $Tb_{18.7V}$-Tb_{89V}, and $Tb_{10.65V}$-$Tb_{10.65H}$ also slightly contributed to the retrieval of the SWE, for example, with the unRMSE values of 78.1, 76.9, and 75.3 mm, respectively, for Scenarios 1–3 (Table IV). For the SNOTEL dataset, $Tb_{18.7V}$-Tb_{89V} even increased the uncertainties of the estimated SWE, for example, with the unRMSE values of 127.7 and 129.8 mm for Scenarios 1 and 2, respectively (Table IV). These results correspond to the analysis in Fig. 12.

According to the results shown in Figs. 13 and 14, SWE retrieval in forested areas still faces challenges. Although the forest fraction was considered in the HUT-RF model to reduce the influence of forests on SWE references, the pixel-based regression algorithms did not compensate for the SWE via the forest cover fraction. For example, the satellite brightness temperature was stable in densely forested areas (Fig. 14), which resulted in an almost static estimated SWE. Thus, it is necessary to implement a forest correction step for the brightness temperature prior to estimating the SWE. From the perspective of radiative transfer, an integrated microwave emission model that considers the influence of the forest landscape is the base method used to correct the satellite brightness temperature. We are now attempting to establish a microwave emission model, in which the advanced integral equation model (AIEM) and HUT are used to simulate soil and snow brightness temperatures, respectively, and a zero-order τ-ω forest model is used to describe canopy self-radiation and interactions with snow and soil [55]. Based on the integrated microwave emission model, we skillfully combined two radiative transfer equations for adjacent forests and open pixels to extract canopy transmissivity. A semiempirical canopy transmissivity model based on forest biomass was then built to correct satellite-observed brightness temperatures. We are now designing an airborne-based observation experiment to evaluate this method. We will expand this methodology to the global scale for satellite applications. The detailed results will be presented in a future publication, and we believe that the forest-corrected brightness temperature will improve the effective grain size and SWE estimates in forested areas.

V. CONCLUSION

In this article, a new operational SWE retrieval algorithm for FY-3F/MWRI-II in the Northern Hemisphere was proposed. The proposed algorithm differs from traditional static methods based on its spatially dynamic regression coefficients. To verify the performance of the FY-3F SWE algorithm, four spatially independent verification datasets across the Northern Hemisphere were used in this study. Moreover, the FY-3F SWE estimates were compared with those of the widely used GlobSnow-v3.0 product. The results showed that the HUT-RF model SWE estimates conformed to the ground-based measurements, but the HUT-RF model relied heavily on ground-based snow depth observations. Thus, a pixel-sensitive FY-3F retrieval algorithm was built based on a spatially continuous SWE reference dataset generated by the HUT-RF. Our verification also revealed that the proposed FY-3F algorithm yielded results similar to those for the GlobSnow-v3.0 product in plain terrains and sparsely forested areas. For example, the unRMSE values over Russia were 27.15 and 33.32 mm for the FY-3F and GlobSnow-v3.0 algorithms, respectively. In complex terrains and densely forested areas, the FY-3F algorithm performed better than the GlobSnow-v3.0 product did, but it also had high uncertainties, with overall unRMSE values of 75.3 mm over Canada and 129.06 mm over western North America. Another advantage of the FY-3F SWE retrieval algorithm is that it can provide SWE information in complex mountains where a mass of snow is stored. Compared with those of the FY-3B/C/D algorithms, the proposed SWE retrieval method for FY-3F yielded consistent results across the Northern Hemisphere, avoiding SWE patches. We also attempt to validate the proposed algorithm against FY-3G/MWRI-RM and FY-3F/MWRI-II observations, which could increase the number of applications of FY-3 series satellites. It is also necessary to compare the differences between FY-3C/MWRI observations and FY-3F/MWRI-II or FY-3G/MWRI-RM observations and then update the proposed algorithm in the future after enough FY-3F/3G-observed brightness temperature products are obtained. Undeniably, the proposed FY-3F algorithm enhances Earth monitoring capabilities and contributes to a complete and timely understanding of SWE changes at the global scale.

REFERENCES

[1] T. P. Barnett, J. C. Adam, and D. P. Lettenmaier, “Potential impacts of a warming climate on water availability in snow-dominated regions,” *Nature*, vol. 438, no. 7066, pp. 303–309, Nov. 2005.

[2] V. A. Bell, A. L. Kay, H. N. Davies, and R. G. Jones, “An assessment of the possible impacts of climate change on snow and peak river flows across Britain,” *Climatic Change*, vol. 136, nos. 3–4, pp. 539–553, Jun. 2016.

[3] X. Qu and A. Hall, “On the persistent spread in snow-albedo feedback,” *Climate Dyn.*, vol. 42, nos. 1–2, pp. 69–81, Jan. 2014.

[4] J. Pulliainen et al., “Early snowmelt significantly enhances boreal springtime carbon uptake,” *Proc. Nat. Acad. Sci. USA*, vol. 114, no. 42, pp. 11081–11086, Oct. 2017.

[5] J. R. Dierauer, D. M. Allen, and P. H. Whitfield, “Snow drought risk and susceptibility in the western United States and southwestern Canada,” *Water Resour. Res.*, vol. 55, no. 4, pp. 3076–3091, Apr. 2019, doi: 10.1029/2018wr023229.

[6] Y. Qin et al., “Agricultural risks from changing snowmelt,” *Nature Climate Change*, vol. 10, no. 5, pp. 459–465, May 2020.

[7] A. Rango, A. T. C. Chang, and J. L. Foster, “The utilization of spaceborne microwave radiometers for monitoring snowpack properties,” *Hydrol. Res.*, vol. 10, no. 1, pp. 25–40, Feb. 1979.

[8] A. T. C. Chang, J. L. Foster, and D. K. Hall, “Nimbus-7 SMMR derived global snow cover parameters,” *Ann. Glaciol.*, vol. 9, pp. 39–44, May 1987.

[9] A. J. Dietz, C. Kuenzer, U. Gessner, and S. Dech, “Remote sensing of snow—A review of available methods,” *Int. J. Remote Sens.*, vol. 33, no. 13, pp. 4094–4134, Jul. 2012.

[10] R. D. Brown and D. A. Robinson, “Northern Hemisphere spring snow cover variability and change over 1922–2010 including an assessment of uncertainty,” *Cryosphere*, vol. 5, no. 1, pp. 219–229, Mar. 2011.

[11] R. Brown, D. Tapsoba, and C. Derksen, “Evaluation of snow water equivalent datasets over the Saint-Maurice river basin region of southern Québec,” *Hydrological Processes*, vol. 32, no. 17, pp. 2748–2764, Aug. 2018.

[12] J. Lemmetyinen et al., “Simulating seasonally and spatially varying snow cover brightness temperature using HUT snow emission model and retrieval of a microwave effective grain size,” *Remote Sens. Environ.*, vol. 156, pp. 71–95, Jan. 2015.

[13] I. Merkouriadi, J. Lemmetyinen, G. E. Liston, and J. Pulliainen, “Solving challenges of assimilating microwave remote sensing signatures with a physical model to estimate snow water equivalent,” *Water Resour. Res.*, vol. 57, no. 11, pp. 1–24, Nov. 2021.

[14] B. J. Vander Jagt, M. T. Durand, S. A. Margulis, E. J. Kim, and N. P. Molotch, “The effect of spatial variability on the sensitivity of passive microwave measurements to snow water equivalent,” *Remote Sens. Environ.*, vol. 136, pp. 163–179, Sep. 2013.

[15] R. E. Kelly, A. T. Chang, L. Tsang, and J. L. Foster, “A prototype AMSR-E global snow area and snow depth algorithm,” *IEEE Trans. Geosci. Remote Sens.*, vol. 41, no. 2, pp. 230–242, Feb. 2003.

[16] R. Kelly, “The AMSR-E snow depth algorithm: Description and initial results,” *J. Remote Sens. Soc. Jpn.*, vol. 29, pp. 307–317, Jan. 2009.

[17] M. Takala et al., “Estimating Northern Hemisphere snow water equivalent for climate research through assimilation of space-borne radiometer data and ground-based measurements,” *Remote Sens. Environ.*, vol. 115, no. 12, pp. 3517–3529, Dec. 2011.

[18] K. Luojus et al., “GlobSnow v3.0 Northern Hemisphere snow water equivalent dataset,” *Sci. Data*, vol. 8, no. 1, pp. 1–16, Jul. 2021.

[19] L. Jiang, P. Wang, L. Zhang, H. Yang, and J. Yang, “Improvement of snow depth retrieval for FY3B-MWRI in China,” *Sci. China Earth Sci.*, vol. 44, pp. 531–547, Jan. 2014.

[20] J. Yang, L. Jiang, S. Wu, G. Wang, J. Wang, and X. Liu, “Development of a snow depth estimation algorithm over China for the FY-3D/MWRI,” *Remote Sens.*, vol. 11, no. 8, p. 977, Apr. 2019.

[21] J. Yang et al., “Snow depth estimation and historical data reconstruction over China based on a random forest machine learning approach,” *Cryosphere*, vol. 14, no. 6, pp. 1763–1778, Jun. 2020.

[22] L. Gu, R. Ren, X. Li, and K. Zhao, “Snow depth retrieval based on a multifrequency passive microwave unmixing method for saline-alkaline land in the western Jilin province of China,” *IEEE J. Sel. Topics Appl. Earth Observ. Remote Sens.*, vol. 11, no. 7, pp. 2210–2222, Jul. 2018.

[23] F. Larue, A. Royer, D. De Sève, A. Langlois, A. Roy, and L. Brucker, “Validation of GlobSnow-2 snow water equivalent over Eastern Canada,” *Remote Sens. Environ.*, vol. 194, pp. 264–277, Jun. 2017.

[24] C. Mortimer et al., “Evaluation of long-term Northern Hemisphere snow water equivalent products,” *Cryosphere*, vol. 14, no. 5, pp. 1579–1594, May 2020.

[25] R. Zhang et al., “Evaluation and adjustment of the AMSR2 snow depth algorithm for the Northern Xinjiang Region, China,” *IEEE J. Sel. Topics Appl. Earth Observ. Remote Sens.*, vol. 10, pp. 3892–3903, 2017.

[26] M. Tedesco and J. Jeyaratnam, “A new operational snow retrieval algorithm applied to historical AMSR-E brightness temperatures,” *Remote Sens.*, vol. 8, no. 12, p. 1037, Dec. 2016.

[27] J. Herbert, M. Raleigh, and E. Small, “Reanalyzing the spatial representativeness of snow depth at automated monitoring stations using airborne LiDAR data,” *EGUsphere*, vol. 2023, pp. 1–27, Nov. 2023, doi: 10.5194/egusphere-2023-2543.

[28] E. H. Bair, A. Abreu Calfa, K. Rittger, and J. Dozier, “Using machine learning for real-time estimates of snow water equivalent in the watersheds of Afghanistan,” *Cryosphere*, vol. 12, no. 5, pp. 1579–1594, May 2018.

[29] E. Santi, S. Pettinato, S. Paloscia, P. Pampaloni, G. Macelloni, and M. Brogioni, “An algorithm for generating soil moisture and snow depth maps from microwave spaceborne radiometers: HydroAlgo,” *Hydrol. Earth Syst. Sci.*, vol. 16, no. 10, pp. 3659–3676, Oct. 2012.

[30] E. Santi et al., “Exploiting the ANN potential in estimating snow depth and snow water equivalent from the airborne SnowSAR data at X- and Ku-bands,” *IEEE Trans. Geosci. Remote Sens.*, vol. 60, 2022, Art. no. 4301216, doi: 10.1109/TGRS.2021.3086893.

[31] E. Santi et al., “On the use of COSMO-SkyMed X-band SAR for estimating snow water equivalent in Alpine areas: A retrieval approach based on machine learning and snow models,” *IEEE Trans. Geosci. Remote Sens.*, vol. 60, 2022, Art. no. 4305419, doi: 10.1109/TGRS.2022.3191409.

[32] N. Saberi, R. Kelly, J. Pan, M. Durand, J. Goh, and K. A. Scott, “The use of a Monte Carlo Markov chain method for snow-depth retrievals: A case study based on airborne microwave observations and emission modeling experiments of Tundra snow,” *IEEE Trans. Geosci. Remote Sens.*, vol. 59, no. 3, pp. 1876–1889, Mar. 2021.

[33] X. Xu, X. Liu, X. Li, Q. Shi, Y. Chen, and B. Ai, “Global snow depth retrieval from passive microwave brightness temperature with machine learning approach,” *IEEE Trans. Geosci. Remote Sens.*, vol. 60, 2022, Art. no. 4302917.

[34] J. Pan et al., “Combination of snow process model priors and site representativeness evaluation to improve the global snow depth retrieval based on passive microwaves,” *IEEE Trans. Geosci. Remote Sens.*, vol. 61, 2023, Art. no. 4301120.

[35] S. Gao et al., “A novel global snow depth retrieval method considering snow metamorphism and forest influence,” *Remote Sens. Environ.*, vol. 295, Sep. 2023, Art. no. 113712.

[36] M. Reichstein et al., “Deep learning and process understanding for data-driven Earth system science,” *Nature*, vol. 566, no. 7743, pp. 195–204, Feb. 2019.

[37] Y. Ma, S. Chen, S. Ermon, and D. B. Lobell, “Transfer learning in environmental remote sensing,” *Remote Sens. Environ.*, vol. 301, Feb. 2024, Art. no. 113924.

[38] J. W. Yang, L. M. Jiang, J. Lemmetyinen, J. M. Pan, K. Luojus, and M. Takala, “Improving snow depth estimation by coupling HUT-optimized effective snow grain size parameters with the random forest approach,” *Remote Sens. Environ.*, vol. 264, Oct. 2021, Art. no. 112630.

[39] M. Menne, I. Durre, R. Vose, B. Gleason, and T. Houston, “An overview of the global historical climatology network-daily database,” *J. Atmos. Ocean. Technol.*, vol. 29, no. 7, pp. 897–910, Jul. 2012.

[40] H. Lievens et al., “Snow depth variability in the Northern Hemisphere mountains observed from space,” *Nature Commun.*, vol. 10, no. 1, p. 4629, Oct. 2019.

[41] H. Lievens, I. Brangers, H.-P. Marshall, T. Jonas, M. Olefs, and G. De Lannoy, “Sentinel-1 snow depth retrieval at sub-kilometer resolution over the European Alps,” *Cryosphere*, vol. 16, no. 1, pp. 159–177, Jan. 2022.

[42] L. Kitaev, A. Kislov, A. Krenke, V. Razuvaev, R. Martuganov, and I. Konstantinov, “The snow characteristics of northern Eurasia and their relationship to climatic parameters,” *Boreal Environ. Res.*, vol. 7, no. 4, p. 437, 2002.

[43] V. Vionnet, C. Mortimer, M. Brady, L. Arnal, and R. Brown, “Canadian historical snow water equivalent dataset (CanSWE, 1928–2020),” *Earth Syst. Sci. Data*, vol. 13, no. 9, pp. 4603–4619, Sep. 2021.

[44] S. W. Fleming, L. Zukiewicz, M. L. Strobel, H. Hofman, and A. G. Goodbody, "SNOTEL, the soil climate analysis network, and water supply forecasting at the natural resources conservation service: Past, present, and future," *JAWRA J. Amer. Water Resour. Assoc.*, vol. 59, no. 4, pp. 585–599, Aug. 2023.

[45] M. Sturm, J. Holmgren, and G. Liston, "A seasonal snow cover classification system for local to global applications," *J. Climate*, vol. 8, no. 5, pp. 1261–1283, May 1995.

[46] C. Derksen, A. Walker, and B. Goodison, "Evaluation of passive microwave snow water equivalent retrievals across the boreal forest/tundra transition of western Canada," *Remote Sens. Environ.*, vol. 96, nos. 3–4, pp. 315–327, Jun. 2005.

[47] J. Dozier, E. H. Bair, and R. E. Davis, "Estimating the spatial distribution of snow water equivalent in the world's mountains," *WIREs Water*, vol. 3, no. 3, pp. 461–474, May 2016.

[48] D. K. Singh, S. Tanniru, K. K. Singh, H. S. Negi, and R. Ramsankaran, "Passive microwave remote sensing based high resolution snow depth mapping for western Himalayan zones using multifactor modelling approach," *Cryosphere Discuss.*, vol. 2023, pp. 1–45, Jun. 2023.

[49] L. Dai, T. Che, L. Xiao, M. Akynbekkyzy, K. Zhao, and L. Leppänen, "Improving the snow volume scattering algorithm in a microwave forward model by using ground-based remote sensing snow observations," *IEEE Trans. Geosci. Remote Sens.*, vol. 60, 2022, Art. no. 4300617.

[50] J. Pulliainen et al., "Patterns and trends of Northern Hemisphere snow mass from 1980 to 2018," *Nature*, vol. 581, no. 7808, pp. 294–298, May 2020.

[51] N. Grody and A. Basist, "Global identification of snow cover using SSM/I measurements," *IEEE Trans. Geosci. Remote Sens.*, vol. 34, no. 1, pp. 237–249, Jan. 1996.

[52] X. Liu, L. Jiang, S. Wu, S. Hao, G. Wang, and J. Yang, "Assessment of methods for passive microwave snow cover mapping using FY-3C/MWRI data in China," *Remote Sens.*, vol. 10, no. 4, p. 524, Mar. 2018.

[53] L. Zschenderlein, K. Luojus, M. Takala, P. Venäläinen, and J. Pulliainen, "Evaluation of passive microwave dry snow detection algorithms and application to SWE retrieval during seasonal snow accumulation," *Remote Sens. Environ.*, vol. 288, Apr. 2023, Art. no. 113476.

[54] C. Derksen, "The contribution of AMSR-E 18.7 and 10.7 GHz measurements to improved boreal forest snow water equivalent retrievals," *Remote Sens. Environ.*, vol. 112, no. 5, pp. 2701–2710, May 2008.

[55] J. Yang, L. Jiang, S. Wu, Y. Luan, J. Pan, and J. Shi, "A semi-empirical microwave transmissivity model for forest canopies during the snow season," *Nat. Remote Sens. Bull.*, vol. 28, no. 4, pp. 981–994, 2024.

Jianwei Yang received the M.S. degree from the University of Chinese Academy of Sciences, Beijing, China, in 2017, and the Ph.D. degree from Beijing Normal University, Beijing, in 2021.

He is currently an Assistant Professor with the Faculty of Geographical Science, Beijing Normal University. His research interests include the interaction of microwaves with snowpacks, microwave remote sensing of the cryosphere, and the development of algorithms for snow parameters, e.g., snow depth, snow water equivalent, and snow density.

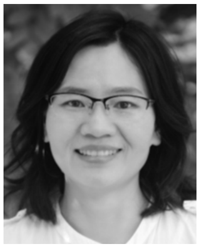

Lingmei Jiang (Member, IEEE) received the Ph.D. degree in geography from Beijing Normal University, Beijing, China, in 2005.

She is currently a Professor with the Faculty of Geographical Science, Beijing Normal University. She has authored or co-authored more than 150 scientific publications. Her research interests include microwave emission/scattering modeling of the land surface, passive microwave remote sensing of the snow water equivalent, soil moisture, and the surface freeze/thaw state.

Dr. Jiang was awarded the Shi Yafeng Prize for Young Scientists in Cryosphere and Environment in 2018.

Zhaojun Zheng received the B.S. degree in atmospheric science from Nanjing University, Nanjing, China, in 2000, and the M.S. degree in atmospheric physics and atmospheric environment from Peking University, Beijing, China, in 2008.

Since 2000, he has been working with the Satellite Meteorological Institute, National Satellite Meteorological Center, China Meteorological Administration, Beijing, where he became a Research Associate in 2009, focusing on cryosphere remote sensing, analysis of cryospheric change and optical cloud mask.

Jinmei Pan (Member, IEEE) received the B.S. and M.S. degrees in cartography and geographic information system from Beijing Normal University, Beijing, China, in 2009 and 2012, respectively, and the Ph.D. degree in geodetic science from The Ohio State University, Columbus, OH, USA, in 2017.

From 2017 to 2023, she was an Assistant Researcher with the State Key Laboratory of Remote Sensing Science, Beijing. In late 2023, she moved to the National Space Science Center, Chinese Academy of Sciences (CAS), Beijing. Her research interests include snow observation, snow water equivalent estimation, and snow hydrology supported by remote sensing techniques and snow process models.

Anaer Shayiran received the bachelor's degree from Sun Yat-sen University, Guangzhou, China, in 2019.

She is currently a Research and Development Engineer with Beijing Huayun Shinetek Science and Technology Company, Ltd., Beijing, China. Her research interests include the microwave remote sensing of the cryosphere and the development of algorithms for cloud microphysical characteristics.